

From Tokens to Photons: Test-Time Physical Prompting for Vision-Language Models

Boyeong Im

Wooseok Lee

Yoojin Kwon

Hyung-Sin Kim*

Seoul National University

{boyn707, andylws, ideastraw, hyungkim}@snu.ac.kr

Abstract

To extend the application of vision-language models (VLMs) from web images to sensor-mediated physical environments, we propose Multi-View Physical-prompt for Test-Time Adaptation (MVP), a forward-only framework that moves test-time adaptation (TTA) from tokens to photons by treating the camera exposure triangle—ISO, shutter speed, and aperture—as physical prompts. At inference, MVP acquires a library of physical views per scene, selects the top- k sensor settings using a source-affinity score, evaluates each retained view under lightweight digital augmentations, filters the lowest-entropy subset of augmented views, and aggregates predictions with Zero-temperature softmax (i.e., hard voting). This selection-then-vote design is simple, calibration-friendly, and requires no gradients or model modifications. On ImageNet-ES and ImageNet-ES-Diverse, MVP consistently outperforms digital-only TTA on single Auto-Exposure captures—by up to 25.6 percentage points (pp)—and delivers up to 3.4 pp additional gains over pipelines that combine conventional sensor control with TTA. MVP remains effective under reduced parameter candidate sets that lower capture latency, demonstrating practicality. These results support the main claim that, beyond post-capture prompting, measurement-time control—selecting and combining real physical views—substantially improves robustness for VLMs.

1. Introduction

Large Vision-Language Models (VLMs), such as CLIP [20], show strong zero-shot generalization and can be further adapted with recent test-time adaptation (TTA) and test-time prompt tuning (TPT). However, as these models move from web-image benchmarks to physical AI settings—mobile assistants, AR devices, and robots [14, 24]—inputs arrive through **controllable sensors**, not just fixed JPEGs. Camera settings (ISO, shutter

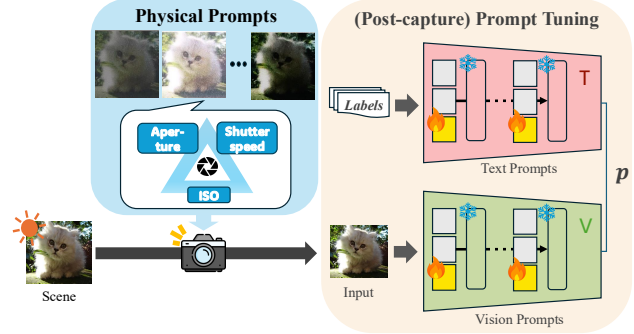


Figure 1. **Conceptual Figure of the Physical Prompts** In the causal chain of scene \rightarrow measurement \rightarrow representation, physical prompts are controlled by sensor parameters (e.g., ISO, shutter speed, aperture) to minimize irrecoverable information loss during measurement, a loss that cannot be compensated by prompt tuning on post-capture images.

speed, aperture) and lighting directly shape the photons that reach the sensor and thus the information available to the image encoder. This raises a natural question: **alongside text and image prompts, can we also guide how a scene is measured at test time for VLMs?**

A growing body of evidence suggests that **scale alone** does not guarantee coverage of the real world’s combinatorial diversity. A recent dataset classification study [18] shows that modern networks can accurately identify which large-scale dataset an image came from—e.g., YFCC [28], CC12M [6], or DataComp [9]—indicating that data collection pipelines leave distinct, learnable fingerprints that **persist** even at Internet scale. This phenomenon revives the classic “*Name That Dataset*” result [29] at a modern scale and aligns with various bias analyses [4, 22, 35], suggesting that training distributions of even large-scale datasets encode stable biases that models reuse at test time.

When VLMs move into sensor-mediated physical deployments, an additional, on-the-fly bias appears: **capture bias**. Sensor parameter choices shift the input data distribution at test time, affecting recognition and calibration. This capture bias compounds the dataset bias already

*Corresponding author.

baked in at pre-training: each test scene is re-sampled from a new micro-distribution determined by how it was measured. However, while these challenges arise at the physical level, most prior work addresses robustness in the digital domain—adapting models to distribution shift *after capture*. Recent TPT methods, which optimize text [8, 19, 26, 31, 36] or both textual and visual prompts [1, 16], and lightweight TTA methods [7, 15, 27, 34] improve generalization on numerous shift benchmarks [10–12, 22, 30], but they remain restricted to the *post-capture* setting. These approaches operate on a fixed physical view, changing how the model interprets an image rather than how the image is acquired. Consequently, they often face a practical limitation: information lost at measurement (e.g., due to lighting or exposure) cannot be fully recovered downstream. When a scene falls outside the operating range determined by lighting and sensor parameters, the appropriate intervention is to change how we measure—not only how we decode.

To address these limitations, we introduce **Multi-View Physical-prompt for Test-Time Adaptation (MVP)**, a *training-free* framework that extends TTA from tokens to photons. At inference, we treat the exposure triangle—ISO, shutter speed, aperture—as **physical prompts** that determine which photons are integrated (Figure 1). Specifically, for each test scene *MVP* acquires a library of M multiple physical views by varying these parameters. For robust scoring, each physical view is additionally evaluated under N lightweight digital augmentations; these do not replace physical views but stabilize selection. For each sensor parameter setting (*i.e.*, the N augmented views of one capture), we compute a *source-affinity score* as the distance between its image features and source-domain feature statistics (lower is better). We then select the top- k sensor settings with the lowest distance (*i.e.*, highest alignment). Among the resulting $k \cdot N$ augmented views, *MVP* further selects those with lowest *predictive entropy* (a confidence filter) and aggregates their predictions with *zero-temperature* softmax (*i.e.*, hard voting), avoiding overconfidence issues of probability averaging across views. Requiring no gradients and no model modifications, *MVP* complements large-scale pre-training by making *measurement-time* choices that reduce irrecoverable information loss and distribution shift before encoding.

Experiments on ImageNet-ES [2] and ImageNet-ES-Diverse [3]—two public benchmarks of static scenes with varying physical illumination and sensor conditions—demonstrate the effectiveness of *MVP*. *MVP* remarkably improves top-1 accuracy by at least **25.58 percentage points (pp)** over applying digital-only TTA/TPT to single-shot Auto-Exposure captures, and further yields up to **3.4 pp** additional gains over pipelines that combine conventional sensor control [3] with digital-level TTA. These results indicate that source-aligned selection of physical

views, coupled with entropy-based filtering and hard-voting aggregation, is more effective than adapting to a single, potentially suboptimal view in a post-capture manner—highlighting the necessity of sensor-level adaptation for VLM deployment in sensor-mediated environments.

In summary, our main contributions are as follows:

- **Sensor-as-prompt for VLMs.** We formulate the exposure triangle (ISO, shutter speed, aperture) as a test-time physical prompt, explicitly integrating sensor control into a VLM test-time adaptation framework.
- **Training-free, forward-only.** *MVP* does not require any gradient update and model modification, relying only on forward passes; it is compatible with parameter-opaque deployments that provide access only to features or logits, preserving applicability to “gray-box” APIs.
- **Dual-criterion selection with calibration-friendly aggregation.** We select views jointly using source-domain feature affinity and predictive confidence, then aggregate with zero-temperature softmax (hard voting), resulting in robust predictions under varying physical environments.
- **Capture-aware evaluation and gains.** On ImageNet-ES and -Diverse, *MVP* substantially outperforms state-of-the-art TTA/TPT baselines on Auto-Exposure single-shot captures and pipelines with conventional sensor control, establishing improvements under capture shift.

2. Related Work

2.1. Prompt Tuning for VLMs

VLMs [13, 20] achieve strong zero-shot performance via large-scale vision–language pre-training. To enhance transferability to downstream tasks, prompt tuning methods introduce learnable vector prompts into the language branch [37, 38] or both language and visual branches [17], but rely on annotated downstream training data.

To address this dependency, Test-Time Prompt Tuning (TPT) [26] adapts a text prompt vector on-the-fly for each *individual test sample* using unsupervised objectives (entropy minimization). Memory- and history-based extensions [19, 31, 36] share information across test samples to mitigate forgetting and cost. However, vanilla entropy minimization can lead to overconfident predictions. To mitigate this issue, C-TPT [33] and O-TPT [25] leverage better-calibrated text features to reduce error. In the visual branch, PromptAlign [1] augments TPT with a token-distribution alignment loss that explicitly encourages test image features to match source-domain statistics, improving robustness under distribution misalignment. Despite not requiring labels, these methods still *backpropagate* to update prompts, making them heavier than forward-only schemes.

2.2. Forward-only Test-Time Adaptation for VLMs

Test-Time Adaptation (TTA) adapts models online to unseen test data. Recent VLM-focused TTA methods [7,

[15, 27, 34] reduce the computation overhead by adopting forward-only updates (no gradients through the encoder). TDA [15] progressively updates a lightweight key-value cache of pseudo-labels and test data features to refine predictions without gradients. MTA [34] adapts directly in the embedding space by aggregating reliable test-time augmented views around a central prototype. ZERO [7] revisits augmentation-based ensembling and shows that view selection and zero-temperature softmax (hard voting) can reduce inference latency relative to backprop-based TPT while remaining competitive: by converting per-view predictions to equal-weight votes, ZERO becomes insensitive to logit-scale inflation across views.

Notably, the standard evaluation protocol for both TPT and TTA is zero-shot image classification, which we adopt for comparability with these baselines.

2.3. Sensor-level Covariate Shifts and Adaptation

Prior TPT/TTA methods primarily address post-capture shifts, operating on a fixed physical view of a test scene and adapting model interpretation rather than how the image is acquired. In contrast, *sensor-level shifts* arise from the interaction of lighting with camera parameters (ISO, shutter speed, aperture). ImageNet-ES [2] and ImageNet-ES-Diverse [3] introduce benchmarks with controlled variations in the light–sensor interaction for static scenes, exposing robustness gaps that digital-only methods cannot fully close. Adaptive sensor control addresses this by changing capture. Lens [3] proposes a post-hoc, camera-agnostic controller that selects sensor settings per scene using model confidence on candidate captures, significantly improving accuracy under capture shift. However, confidence-only selection can remain vulnerable to overconfidence.

Building upon these insights, our method differs in three ways: (1) we add a source-domain feature-affinity criterion to guide domain-aligned selection of physical views; (2) we aggregate predictions using zero-temperature hard voting rather than probability averaging; and (3) we integrate selection and aggregation into a forward-only, online VLM adaptation pipeline. To our knowledge, this is the first study of the interplay between TTA and adaptive sensor control for VLMs, explicitly leveraging physical multiviews instead of only synthetic augmentations.

3. Methodology

Modern TTA methods for VLMs operate *after capture*, adjusting how the model interprets a fixed image. With Auto-Exposure (AE), however, the captured scene may already have lost information (e.g., saturation or low photon count). In such cases, digital TTA faces a hard practical bound: once photons are not measured, downstream adaptation often cannot recover them. This motivates a *sensor-aware* view of test-time adaptation that respects the causal chain:

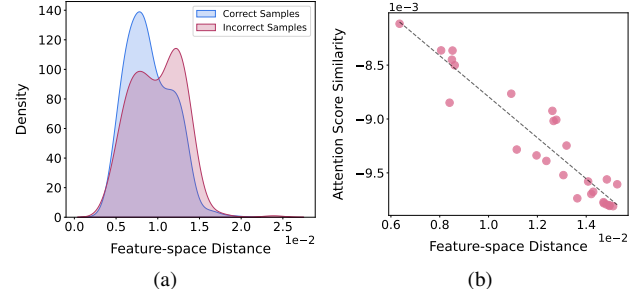


Figure 2. **Motivating findings.** (a) Incorrect samples among Lens top-1 predictions form a bi-modal distribution, with a larger mode skewed toward the higher feature-space distances compared to the correct samples. (b) A strong correlation between attention score similarity and feature-space distance shows that samples closer in feature space exhibit more similar attention patterns.

scene → measurement → representation.

We therefore treat camera sensor parameters—ISO, shutter speed, and aperture—as *physical prompts*: upstream control variables that determine which photons reach the sensor, analogous to how text prompts steer embeddings and visual prompts nudge feature extraction.

3.1. Motivations for Source Affinity Criterion

A natural baseline is to combine an existing sensor-control policy [3] (confidence-based selection of a single capture) with digital TTA. However, confidence-only selection can be brittle when the model is confidently wrong on shifted views. Figure 2a illustrates such failure modes: under a single lighting condition (L1) of ImageNet-ES-Diverse [3], we measure the feature-space distance between most-confident physical views and the source image, revealing that incorrect samples tend to lie farther from the source distribution while correct samples skew toward smaller distances.

Our key insight is to inject a feature-space criterion into the physical-view selection pipeline. Inspired by PromptAlign [1]—which improves zero-shot behavior by bringing test statistics closer to source statistics—we extend the idea upstream: among multiple physical views of the same scene, prefer those whose feature statistics are closest to the source distribution. Intuitively, these views let the model “see” the scene in a way that resembles its pre-training regime, enabling its zero-shot prior to work as intended.

Figure 2b supports this intuition: as the feature-space distance of ImageNet-ES-Diverse parameter settings to the source scene decreases, the attention score similarity increases as well, meaning that the model attends to the physical view’s local visual cues in a more source-aligned manner. Figure 3 offers a complementary visualization. We compare attention maps for images of the same scene—the source (ImageNet) and various sensor-parameter selections from ImageNet-ES-Diverse, including Auto-Exposure views, confidence-based samples, and distance-based samples. The distance-based selections exhibit attention pat-

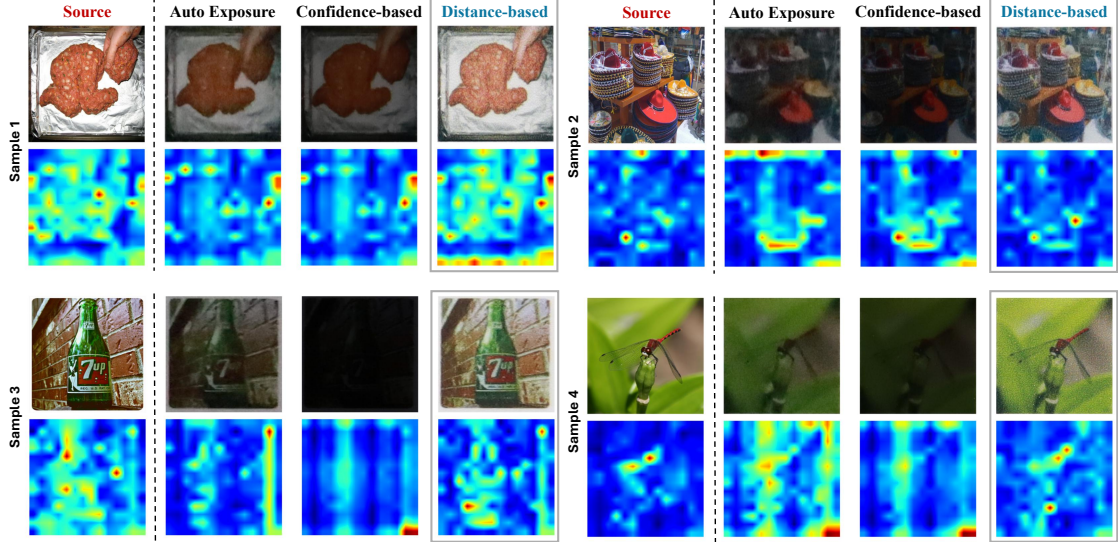


Figure 3. **Visualization of attention maps from different camera parameters.** From the identical scene, we compare the attention maps of the source image (ImageNet) and varying parameter samples (ImageNet-ES-Diverse).

terns most similar to the source, clearly distinguishing them from the other views, especially those chosen by the confidence-only strategy (Lens [3]).

3.2. Multi-View Physical-prompt for Test-Time Adaptation

Selecting physical views in feature-space. Figure 4 illustrates the overall pipeline of *MVP*. Instead of a single AE capture in the conventional pipeline, *MVP* obtains M different physical captures of the same scene under different camera parameter settings and identifies those that are most aligned with the source representation. Each physical capture $v_i \in \mathcal{V} = \{v_1, v_2, \dots, v_M\}$ is further expanded into a set of N digital augmentations $\{v_{i,1}, \dots, v_{i,N}\}$, including the original view itself.

For each capture v_i , we derive N' confident augmentations by selecting the top α fraction of N total augmentations based on confidence. Then, for each layer l , we extract the feature-level mean and variance of image token embedding $\mu_{i,l} = \frac{1}{N'} \sum_{n=1}^{N'} \mu_{i,l,n}$; $\sigma_{i,l}^2 = \frac{1}{N'} \sum_{n=1}^{N'} \sigma_{i,l,n}^2$ from the frozen visual encoder using N' views. These statistics are then compared against the pre-computed source data statistics $(\mu_{s,l}, \sigma_{s,l}^2)$. We use ImageNet as a proxy source dataset to approximate the feature statistics of CLIP’s source distribution, following [1], as the original CLIP pretraining data, containing over 400M image–text pairs, is not publicly released and CLIP has demonstrated strong zero-shot performance on ImageNet.

To measure the similarity of physical views with source image in feature-space, a source-affinity score is defined as:

$$S_i = -\frac{1}{L} \sum_{l=1}^L (\|\mu_{i,l} - \mu_{s,l}\|_2^2 + \|\sigma_{i,l}^2 - \sigma_{s,l}^2\|_2^2), \quad (1)$$

where L denotes the number of layers of the visual encoder. We then select the top- k parameter settings with the largest S_i , corresponding to the physical views that are most consistent with the source data distribution. We realize the spirit of prompt-based distribution alignment without gradient updates by replacing visual-prompt optimization with *physical-prompt selection*, preserving gray-box compatibility and low computational cost.

Entropy-based filtering for augmented views. Even among the top- k physical parameters selected in the previous step, some augmented samples may produce uncertain or noisy predictions due to local variations in illumination or visual context. To mitigate the negative impact of unreliable samples, we measure how uncertain the model is to each augmented view using the Shannon entropy [23]:

$$H_{i,n} = - \sum_c p_{i,n}(c) \log p_{i,n}(c), \quad (2)$$

where $p_{i,n}(c)$ denotes the predicted probability of class c for the n -th digital augmentation of the i -th physical capture. Across all $k \times N$ augmented views obtained from the selected k physical captures, we retain only the bottom $\gamma\%$ in entropy as the most confident subset \mathcal{F} .

The predictions of these entropy-filtered views are then aggregated using a zero-temperature softmax [7], which is equivalent to a hard voting scheme across all selected views:

$$\hat{y} = \arg \max_{y \in \mathcal{C}} \sum_{(i,n) \in \mathcal{F}} \mathbf{1} \left[\arg \max_{c \in \mathcal{C}} p_{i,n}(c) = y \right], \quad (3)$$

where \mathcal{C} is the set of class labels. This aggregation strategy mitigates the overconfidence issues commonly ob-

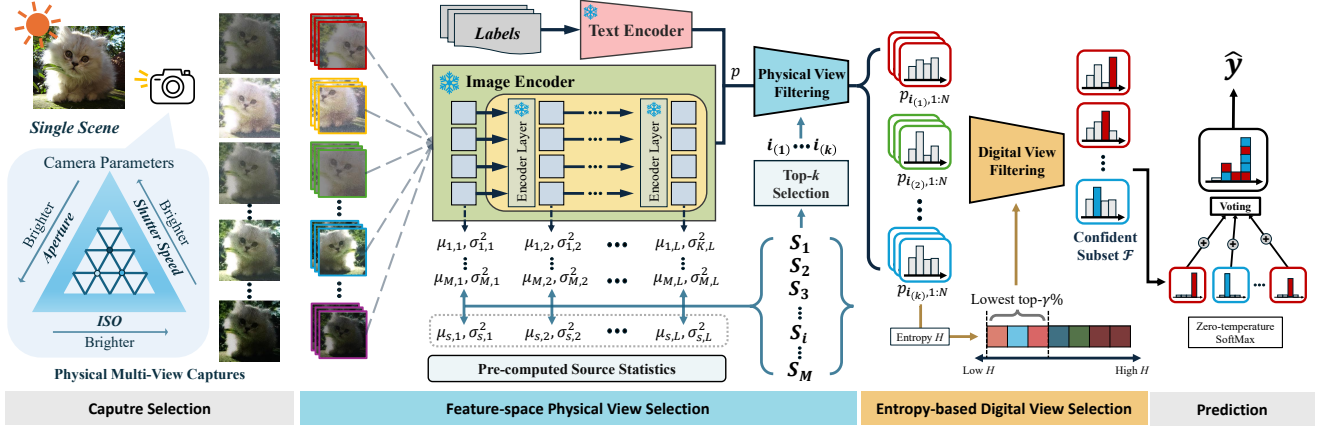


Figure 4. **Overall Framework.** Given a single scene, multiple physical captures are obtained by varying camera parameters along the exposure triangle—ISO, shutter speed, and aperture—forming a set of physical multi-views, as controllable physical prompts.

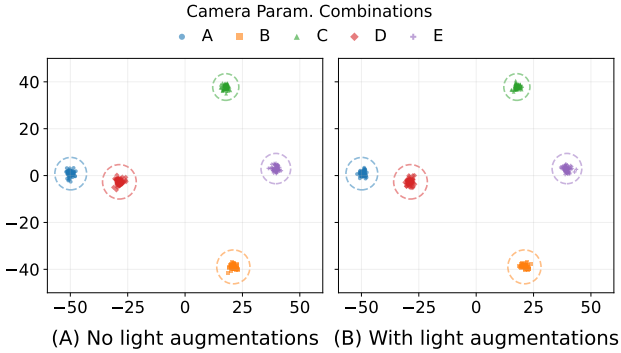


Figure 5. **LDA projection of visual embeddings from five physical views.** (Left) With digital transformation such as Random Crop or Horizontal Flip. (Right) With additional photometric augmentations such as perturbing hue, saturation, and brightness. Visualizations for more samples can be found in the Appendix.

served when averaging softmax probabilities across multiple views, while preserving the robustness gained from physical multiview observations.

3.3. Physical Multiviews as Augmentations

We select not a single sensor configuration but a nearest- k set of camera parameters according to our source-affinity score. Retaining multiple physical views acts as a form of regularization, introducing a physical augmentation axis largely *orthogonal* to digital geometric augmentations (e.g., cropping, flipping) and also distinct from digital photometric augmentations (e.g., contrast, hue).

Figure 5 shows the new dimension of variability granted by different physical augmentations in the representation space. For a scene captured with selected top-5 camera parameters, we project the visual embeddings of their digitally augmented views using LDA. In the left panel, when applying only digital geometric augmentations which are common in VLM TTA, embeddings remain confined within sensor-specific regions. By contrast, changing camera pa-

rameters shifts embeddings into distinct regions, indicating that sensor variation provides an augmentation effect absent in digital transformations. The right panel shows that adding digital photometric augmentations [5] likewise fails to escape these sensor-specific boundaries. Therefore, physical capture diversity realizes a new axis that digital augmentation cannot emulate, enabling the model to perceive the same scene in meaningfully different ways. Selecting a top- k set thus introduces additional degrees of freedom along the new axis and enables more robust predictions through hard voting than relying on a single parameter.

4. Experiments

4.1. Experimental Setup

Datasets. We evaluate our method on two sensor-level shift benchmarks, ImageNet-ES [2] and ImageNet-ES-Diverse [3], both constructed from Tiny-ImageNet [32]. Each dataset contains (i) an *Auto-Exposure (AE)* subset, where scenes are captured several times using the camera’s default exposure setting, and (ii) a *Parameter-Controlled* subset, where the same scenes are recorded under systematically varied ISO, shutter speed, and aperture combinations across multiple lighting environments. This design enables controlled evaluation of sensor-induced covariate shifts. Further capture details are provided in the Appendix.

Baselines. We compare *MVP* to representative approaches across three categories. (1) Prompt learning methods, including CoOp [38] and MaPLe [17], which optimize learnable context tokens for downstream adaptation. We use the publicly released pretrained weights of CoOp and MaPLe without any additional training. (2) Prompt-based TTA methods, including TPT [26], C-TPT [25], O-TPT [33] and PromptAlign [1], which optimize context vectors. (3) Training-free, forward-only TTA methods, including MTA [34], TDA [15], and ZERO [7]. To ensure a

Table 1. **Comparison of vision-language adaptation methods across two datasets: ImageNet-ES and ImageNet-ES-Diverse.** All experiments are conducted using the **ViT-B/16 backbone initialized from MaPLe pretrained weights**. For *Auto Exposure Setting*, models are evaluated without sensor control. For *with Lens*, all tuning-based methods are applied after sensor control via Lens [3]. Results are reported across light environments and detailed per-light environment results are provided in the Appendix.

	Method	Tiny-ImageNet	ImageNet-ES			ImageNet-ES-Diverse		
			AE	AE + Photo Aug.*	with Lens	AE	AE + Photo Aug.*	with Lens
Pre-trained	CLIP [20]	87.6	48.98	-	82.45	37.65	-	61.13
Prompt Learning	CoOp [38]	89.2	51.82	-	84.90	40.47	-	65.15
	MaPLe [17]	89.0	52.57	-	84.40	39.47	-	64.68
Prompt-based TTA	TPT [26]	89.5	55.66	49.66	84.45	41.20	40.82	64.90
	PromptAlign [1]	90.0	55.45	50.27	84.75	41.51	41.04	64.90
	C-TPT [33]	90.5	53.55	45.92	84.55	39.88	39.09	64.72
	O-TPT [25]	89.3	52.70	44.56	84.50	39.14	38.47	64.63
Training-free TTA	MTA [34]	90.6	56.56	54.64	84.70	41.70	41.33	65.08
	TDA [15]	90.0	58.17	57.29	84.80	40.78	40.83	64.85
	ZERO [7]	90.6	57.05	56.77	84.80	39.91	39.80	64.67
<i>MVP</i> (ours)		-		87.85			67.28	

fair comparison with PromptAlign, we initialize the prompt vectors of all methods with the pretrained MaPLe weights. In addition, we include Lens [3] as the sensor-control counterparts, using only the most confident physical capture for each scene based on model predictions.

Evaluation protocols. For each scene, we evaluate all baselines under three sensor-control settings: (1) Auto-Exposure (AE): Without any sensor control, the results are obtained by averaging all five AE captures. (2) AE with digital photometric augmentation: For the same AE captures, additional photometric augmentations (*i.e.*, hue, saturation, brightness) [5] are incorporated into the augmentation process within each TTA pipeline to simulate diverse exposure variations. (3) Lens-based selection: following the procedure in [3], we first identify the most confident physical view among 27 candidates using CLIP-based MaPLe inference, then apply each baseline method to the selected view.

Implementation details. We implement *MVP* upon MaPLe [17], the multi-modal prompting model with the CLIP ViT-B/16 backbone. We additionally implement and evaluate on other models in the Appendix. Source-affinity score is computed for a depth of three layers of the visual encoder ($L = 3$), while the source dataset statistics are pre-computed on ImageNet. For each physical view, we generate 63 digitally augmented views using random resized cropping and horizontal flipping, forming a batch of $N = 64$ digitally augmented images including the original as in prior TTA methods. We use the fraction $\alpha = 0.3$ to include only confident augmentation samples in source-affinity score aggregation. We select the top-5 parameter settings (*i.e.*, $k=5$) with the largest source-affinity score, and within their augmented samples, retain the bottom $\gamma=3\%$ in

entropy as confident predictions for voting.

4.2. Results

Main evaluation. We investigate the effectiveness of *MVP* against post-capture TTA baselines on ImageNet-ES [2] and ImageNet-ES-Diverse [3]. Table 1 summarizes the results across the three sensor evaluation protocols in Section 4.1. Under AE settings, the zero-shot CLIP model exhibits significantly degraded performance in various lighting conditions, and existing TTAs marginally improve these results. This indicates that adaptation solely on post-captured images cannot compensate for sensor-level information loss. Integrating the digital photometric augmentations, which simulate more various lighting and exposure settings, was also ineffective at improving baseline performances, with O-TPT even decreasing by up to 8.14 pp on ImageNet-ES. This outcome confirms that digital-level perturbations cannot fully reproduce the physical variations induced by camera parameter changes and in some cases, even hinders adaptation.

In contrast, *MVP* outperforms all AE-based TTA settings, increasing at least **29.68 pp** and **25.58 pp** gains, on ImageNet-ES and ImageNet-ES-Diverse, respectively. This highlights the critical need for TTA strategies that explicitly incorporate sensor-level diversity at capture time. We also yield a robust performance improvement by up to **3.4 pp** over the pipelines that combine Lens with TTA methods, demonstrating the efficacy of multiple physical parameters. These findings emphasize that *MVP* further mitigates the sensitivity to suboptimal sensor settings and enhances overall robustness under sensor-level shifts.

Table 2. **Model Performance Across Different Capture Scenarios (CSA).** Without CSA, the capture latency is the full ImageNet-ES setting – 2.41 seconds per scene. For CSA1 / CSA2 / CSA3 [3], the number of captures, M is 12 / 6 / 21, respectively. Lens and all other TTAs are performed based on MaPLe.

Method	CSA 1 (1.06 sec)		CSA 2 (0.37 sec)		CSA 3 (0.91 sec)	
	IN-ES	IN-ES -Diverse	IN-ES	IN-ES -Diverse	IN-ES	IN-ES -Diverse
Lens	84.75	61.79	84.38	61.76	85.00	54.38
+ TPT	84.88	62.22	84.55	62.49	85.05	62.29
+ PromptAlign	84.95	62.03	84.32	62.56	85.25	62.37
+ C-TPT	84.85	61.90	84.68	61.83	85.10	61.91
+ O-TPT	84.77	61.66	84.42	61.27	85.03	61.77
+ MTA	85.37	62.44	85.10	62.74	85.33	62.62
+ TDA	85.30	61.71	84.70	62.08	85.28	62.33
+ ZERO	85.43	61.49	84.60	61.96	85.62	61.69
<i>MVP</i> (ours)	87.27	63.79	86.65	63.79	87.87	64.41

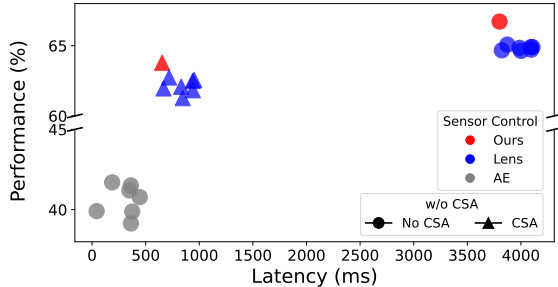


Figure 6. **Latency (ms) of adaptation and inference.** Experiments were conducted on NVIDIA RTX 4090 GPU and Intel(R) Xeon(R) Gold 6326 CPU. Color denotes the sensor control strategy, and markers distinguish TTA variant under the same strategy.

Evaluation with limited parameter settings. While the number of combinations of possible camera parameter grows exponentially, capturing all configurations is impractical due to the associated capture cost and time. To mitigate the inefficiency of the redundant physical capturing, we additionally evaluate our method using Candidate Selection Algorithms (CSA) [3], which is a pre-selection strategy that reduces the candidate space of sensor parameters to a determined set of grids (i.e., smaller M). Table 2 evaluates the three CSA policies in [3]. Across different CSA strategies, *MVP* consistently delivers higher accuracies than other baselines, demonstrating its robustness to limited sensor-control diversity and its scalability to the reduced capture regimes. Consequently, *MVP* achieves a favorable balance between capture efficiency and adaptation performance, making it a practical choice for real-world deployment, especially where capture cost is non-negligible. Details on the CSA policies and full results across different M are provided in the Appendix.

Runtime latency. Figure 6 illustrates the runtime latency (ms)—including capture time, adaptation, and inference—



Figure 7. **Qualitative comparisons with the conventional sensor-control method.**

per test sample, showing that *MVP* delivers a more effective trade-off between performance and latency than the baselines. Specifically, AE attains the lowest latency but the weakest accuracy, consistent with its optimization for human perception rather than model compatibility. Without CSA ($M = 27$ physical views), both *MVP* and Lens exhibit the expected latency–accuracy trade-off relative to AE, delivering ≥ 23.3 pp higher top-1 accuracy at roughly $4\times$ latency, reflecting the cost of capturing 27 physical views per scene. Notably, when CSA is applied ($M = 6$), *MVP* (red triangle) maintains high performance even at low latency, similar to AE settings. Compared to Lens-applied TTA settings (blue markers), *MVP* achieves the highest accuracy at lower latency than competing baselines, demonstrating its strong efficiency–adaptability balance.

Qualitative results. Figure 7 presents confident, digitally-augmented views selected for the final prediction by ZERO with Lens and *MVP*, respectively. *MVP* avoids being trapped by mistakenly selected overconfident physical view in the capture time by considering various physical settings in terms of the model’s perception and delivers optically improved images. It is noteworthy that the lack of the diversity introduced by a limited physical sensor space in a conventional sensor-control approach cannot be mitigated solely by digitally augmented views. Additional results are provided in the Appendix.

5. Ablation Study

Effect of varying k . We examine how the number of physical views selected by the source-affinity score affects accuracy. Figure 8a shows an inverted U-shaped relationship between k and performance. With a fixed confidence percentile $\gamma = 3\%$ (red), increasing k raises the total number of augmented views that enter the vote; when k is too small, the ensemble has too few voters, leading to unstable

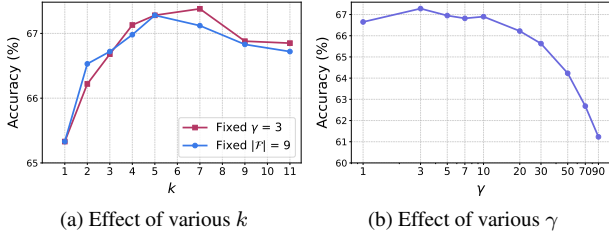


Figure 8. **Ablation on parameter-view selection in *MVP*.** (a) shows the selection of top- k physical parameter settings based on the source-affinity score, while (b) illustrates the confidence percentile thresholding used to filter augmented views for final prediction. We fix $k = 5$ and vary γ from 1% to 90%.

predictions. To decouple the effect of k from the number of voters, we also hold the total count of selected augmented views constant at $|\mathcal{F}| = 9$ (blue). In this setting, smaller k allocates more augmentations per physical view, allowing lower-confidence augmentations to participate in the vote. Conversely, once k exceeds the plateau, accuracy declines slightly because additional, lower-source-affinity physical views are admitted and their associated (often overconfident) augmentations introduce noise that dilutes the vote.

Effect of varying γ . Figure 8b reports the effect of varying the entropy filtering threshold γ , which determines the proportion of digitally augmented views selected for the final aggregation. As shown, the performance peaks at $\gamma = 3\%$ and remains relatively stable up to $\gamma = 10\%$, after which it sharply degrades, indicating that including too many high-entropy (less confident) views introduces noise into the aggregation process, resulting in unstable predictions.

Number of physical views. Table 3 highlights the importance of leveraging multiple physical views rather than relying on a single capture or digital-level augmentations. Aggregating predictions from multiple physical captures consistently outperforms applying digital geometric or additional photometric augmentations to a single physical capture. This demonstrates that using multiple physical views leads to more robust and stable predictions than depending on a single parameter setting. Moreover, even when photometric augmentations are added to the single physical view, the performance still falls short of our approach, underscoring the inherent limitation of digital-level augmentations in simulating sensor-level diversity.

Source-affinity score measurement layers. We evaluate the overall performance by varying the choice of layers for measuring feature-space source affinity score, as summarized in Table 4. It shows that using early layers, particularly the first to third layers, achieves the best accuracy on both datasets. In contrast, computing the score over all layers or only the later layers leads to a significant performance degradation. By measuring the affinity in early-layer feature space, our method can more reliably identify physical views that the model perceives as closer to its pre-training

Table 3. **Ablation Study on Key Design Choices.** Comparison across digital (geometric/photometric) augmentations and physical augmentations using multiple camera parameter views. A total of 320 augmented views are produced per scene for $k=1$ settings, matching the number of those at $k=5$ setting; $64 \times 5 = 320$ views.

Number of top physical views (k)	Digital geo. aug.	Digital photo. aug.	Physical aug.	IN-ES	IN-ES-Diverse
$k = 1$	O	X	X	86.90	66.72
$k = 1$	O	O	X	86.85	66.62
Ours ($k = 5$)	O	X	O	87.85	67.28

Table 4. **Ablation on layer depth for source-affinity score.**

Layer	IN-ES	IN-ES-Diverse	Latency (s)
1-3 (Ours)	87.65	67.25	1.22
	87.85	67.28	1.32
	82.65	18.22	1.40
	82.55	18.85	1.35
12	82.75	20.02	1.40

domain—effectively providing inputs that are “familiar” to the model. In contrast, later layers encode highly semantic representations, making them less transferable across variations in illumination or sensor parameters. As a result, source-affinity scores from these layers provide less reliable cues about their affinity to the source distribution.

6. Conclusion

In this paper, we introduce *MVP*, a novel framework that integrates sensor control into the TTA paradigm by interpreting the camera exposure triangle—ISO, shutter speed, and aperture—as a *physical prompt* for VLMs. By treating the sensor as a controllable prompt, our approach enables the model to decide *what to capture*, extending conventional post-capture TTA into the sensor domain. Extensive experiments on ImageNet-ES and ImageNet-ES-Diverse confirm that our approach consistently outperforms existing Auto-Exposure and Lens-based TTA baselines while maintaining high efficiency even under reduced capture budgets. These results highlight that achieving robust real-world generalization for VLMs requires adapting not only how to interpret visual inputs, but also what to measure.

Limitations and future work. While *MVP* operates in a fully forward-only manner and demonstrates strong robustness, it still requires more than k physical captures per scene as well as pre-computed source-domain statistics. Future work includes extending the framework beyond static scenes and the restricted parameter space considered in this work—toward dynamic environments and broader regions of the exposure parameter manifold. Moreover, applying the proposed physical-prompting paradigm to tasks beyond classification (e.g., detection, retrieval, or semantic segmentation) represents a promising direction.

References

[1] Jameel Abdul Samad, Mohammad Hanan Gani, Noor Hussein, Muhammad Uzair Khattak, Muhammad Muzammal Naseer, Fahad Shahbaz Khan, and Salman H Khan. Align your prompts: Test-time prompting with distribution alignment for zero-shot generalization. *Advances in Neural Information Processing Systems*, 36:80396–80413, 2023. [2](#), [3](#), [4](#), [5](#), [6](#), [11](#)

[2] Eunsu Baek, Keondo Park, Jiyo Kim, and Hyung-Sin Kim. Unexplored faces of robustness and out-of-distribution: Covariate shifts in environment and sensor domains. In *Proceedings of the IEEE/CVF Conference on Computer Vision and Pattern Recognition*, pages 22294–22303, 2024. [2](#), [3](#), [5](#), [6](#), [11](#), [13](#)

[3] Eunsu Baek, Sunghwan Han, Taesik Gong, and Hyung-Sin Kim. Adaptive camera sensor for vision models. *arXiv preprint arXiv:2503.02170*, 2025. [2](#), [3](#), [4](#), [5](#), [6](#), [7](#), [11](#), [12](#), [13](#)

[4] Andrei Barbu, David Mayo, Julian Alverio, William Luo, Christopher Wang, Dan Gutfreund, Josh Tenenbaum, and Boris Katz. Objectnet: A large-scale bias-controlled dataset for pushing the limits of object recognition models. *Advances in neural information processing systems*, 32, 2019. [1](#)

[5] Alexander Buslaev, Vladimir I Iglovikov, Eugene Khvedchenya, Alex Parinov, Mikhail Druzhinin, and Alexandr A Kalinin. Alumentations: fast and flexible image augmentations. *Information*, 11(2):125, 2020. [5](#), [6](#)

[6] Soravit Changpinyo, Piyush Sharma, Nan Ding, and Radu Soricut. Conceptual 12m: Pushing web-scale image-text pre-training to recognize long-tail visual concepts. In *Proceedings of the IEEE/CVF conference on computer vision and pattern recognition*, pages 3558–3568, 2021. [1](#)

[7] Matteo Farina, Gianni Franchi, Giovanni Iacca, Massimiliano Mancini, and Elisa Ricci. Frustratingly easy test-time adaptation of vision-language models. *Advances in Neural Information Processing Systems*, 37:129062–129093, 2024. [2](#), [3](#), [4](#), [5](#), [6](#)

[8] Chun-Mei Feng, Kai Yu, Yong Liu, Salman Khan, and Wangmeng Zuo. Diverse data augmentation with diffusions for effective test-time prompt tuning. In *Proceedings of the IEEE/CVF International Conference on Computer Vision*, pages 2704–2714, 2023. [2](#)

[9] Samir Yitzhak Gadre, Gabriel Ilharco, Alex Fang, Jonathan Hayase, Georgios Smyrnis, Thao Nguyen, Ryan Marten, Mitchell Wortsman, Dhruba Ghosh, Jieyu Zhang, et al. Datacom: In search of the next generation of multimodal datasets. *Advances in Neural Information Processing Systems*, 36:27092–27112, 2023. [1](#)

[10] Dan Hendrycks and Thomas Dietterich. Benchmarking neural network robustness to common corruptions and perturbations. *arXiv preprint arXiv:1903.12261*, 2019. [2](#)

[11] Dan Hendrycks, Steven Basart, Norman Mu, Saurav Kadavath, Frank Wang, Evan Dorundo, Rahul Desai, Tyler Zhu, Samyak Parajuli, Mike Guo, et al. The many faces of robustness: A critical analysis of out-of-distribution generalization. In *Proceedings of the IEEE/CVF international conference on computer vision*, pages 8340–8349, 2021.

[12] Dan Hendrycks, Kevin Zhao, Steven Basart, Jacob Steinhardt, and Dawn Song. Natural adversarial examples. In *Proceedings of the IEEE/CVF conference on computer vision and pattern recognition*, pages 15262–15271, 2021. [2](#)

[13] Chao Jia, Yafei Yang, Ye Xia, Yi-Ting Chen, Zarana Parekh, Hieu Pham, Quoc Le, Yun-Hsuan Sung, Zhen Li, and Tom Duerig. Scaling up visual and vision-language representation learning with noisy text supervision. In *International conference on machine learning*, pages 4904–4916. PMLR, 2021. [2](#)

[14] Gi-Cheon Kang, Junghyun Kim, Kyuhwan Shim, Jun Ki Lee, and Byoung-Tak Zhang. Clip-rt: Learning language-conditioned robotic policies from natural language supervision. *arXiv preprint arXiv:2411.00508*, 2024. [1](#)

[15] Adilbek Karmanov, Dayan Guan, Shijian Lu, Abdulmotaleb El Saddik, and Eric Xing. Efficient test-time adaptation of vision-language models. In *Proceedings of the IEEE/CVF Conference on Computer Vision and Pattern Recognition*, pages 14162–14171, 2024. [2](#), [3](#), [5](#), [6](#)

[16] Anant Khandelwal. Promptsync: Bridging domain gaps in vision-language models through class-aware prototype alignment and discrimination. In *Proceedings of the IEEE/CVF Conference on Computer Vision and Pattern Recognition*, pages 7819–7828, 2024. [2](#)

[17] Muhammad Uzair Khattak, Hanoona Rasheed, Muhammad Maaz, Salman Khan, and Fahad Shahbaz Khan. Maple: Multi-modal prompt learning. In *Proceedings of the IEEE/CVF conference on computer vision and pattern recognition*, pages 19113–19122, 2023. [2](#), [5](#), [6](#), [11](#), [12](#)

[18] Zhuang Liu and Kaiming He. A decade’s battle on dataset bias: Are we there yet? In *The Thirteenth International Conference on Learning Representations*. [1](#)

[19] Xiaosong Ma, Jie Zhang, Song Guo, and Wenchao Xu. Swapprompt: Test-time prompt adaptation for vision-language models. *Advances in Neural Information Processing Systems*, 36:65252–65264, 2023. [2](#)

[20] Alec Radford, Jong Wook Kim, Chris Hallacy, Aditya Ramesh, Gabriel Goh, Sandhini Agarwal, Girish Sastry, Amanda Askell, Pamela Mishkin, Jack Clark, et al. Learning transferable visual models from natural language supervision. In *International conference on machine learning*, pages 8748–8763. PMLR, 2021. [1](#), [2](#), [6](#)

[21] Maithra Raghu, Thomas Unterthiner, Simon Kornblith, Chiyuan Zhang, and Alexey Dosovitskiy. Do vision transformers see like convolutional neural networks? *Advances in neural information processing systems*, 34:12116–12128, 2021. [11](#)

[22] Benjamin Recht, Rebecca Roelofs, Ludwig Schmidt, and Vaishaal Shankar. Do imagenet classifiers generalize to imagenet? In *International conference on machine learning*, pages 5389–5400. PMLR, 2019. [1](#), [2](#)

[23] Claude E Shannon. A mathematical theory of communication. *The Bell system technical journal*, 27(3):379–423, 1948. [4](#)

[24] Rui Shao, Wei Li, Lingsen Zhang, Renshan Zhang, Zhiyang Liu, Ran Chen, and Liqiang Nie. Large vlm-based vision-language-action models for robotic manipulation: A survey. *arXiv preprint arXiv:2508.13073*, 2025. 1

[25] Ashshak Sharifdeen, Muhammad Akhtar Munir, Sanoojan Baliah, Salman Khan, and Muhammad Haris Khan. O-pt: Orthogonality constraints for calibrating test-time prompt tuning in vision-language models. In *Proceedings of the Computer Vision and Pattern Recognition Conference*, pages 19942–19951, 2025. 2, 5, 6

[26] Manli Shu, Weili Nie, De-An Huang, Zhiding Yu, Tom Goldstein, Anima Anandkumar, and Chaowei Xiao. Test-time prompt tuning for zero-shot generalization in vision-language models. *Advances in Neural Information Processing Systems*, 35:14274–14289, 2022. 2, 5, 6

[27] Elaine Sui, Xiaohan Wang, and Serena Yeung-Levy. Just shift it: Test-time prototype shifting for zero-shot generalization with vision-language models. In *2025 IEEE/CVF Winter Conference on Applications of Computer Vision (WACV)*, pages 825–835. IEEE, 2025. 2, 3

[28] Bart Thomee, David A Shamma, Gerald Friedland, Benjamin Elizalde, Karl Ni, Douglas Poland, Damian Borth, and Li-Jia Li. Yfcc100m: The new data in multimedia research. *Communications of the ACM*, 59(2):64–73, 2016. 1

[29] Antonio Torralba and Alexei A Efros. Unbiased look at dataset bias. In *CVPR 2011*, pages 1521–1528. IEEE, 2011. 1

[30] Haohan Wang, Songwei Ge, Zachary Lipton, and Eric P Xing. Learning robust global representations by penalizing local predictive power. *Advances in neural information processing systems*, 32, 2019. 2

[31] Zehao Xiao, Shilin Yan, Jack Hong, Jiayin Cai, Xiaolong Jiang, Yao Hu, Jiayi Shen, Qi Wang, and Cees GM Snoek. Dynaprompt: Dynamic test-time prompt tuning. *arXiv preprint arXiv:2501.16404*, 2025. 2

[32] Xuan Yang. Tiny imagenet visual recognition challenge. 5

[33] Hee Suk Yoon, Eunseop Yoon, Joshua Tian Jin Tee, Mark Hasegawa-Johnson, Yingzhen Li, and Chang D Yoo. C-pt: Calibrated test-time prompt tuning for vision-language models via text feature dispersion. *arXiv preprint arXiv:2403.14119*, 2024. 2, 5, 6

[34] Maxime Zanella and Ismail Ben Ayed. On the test-time zero-shot generalization of vision-language models: Do we really need prompt learning? In *Proceedings of the IEEE/CVF Conference on Computer Vision and Pattern Recognition*, pages 23783–23793, 2024. 2, 3, 5, 6

[35] Boya Zeng, Yida Yin, and Zhuang Liu. Understanding bias in large-scale visual datasets. *Advances in Neural Information Processing Systems*, 37:61839–61871, 2024. 1

[36] Jingyi Zhang, Jiaxing Huang, Xiaoqin Zhang, Ling Shao, and Shijian Lu. Historical test-time prompt tuning for vision foundation models. *Advances in Neural Information Processing Systems*, 37:12872–12896, 2024. 2

[37] Kaiyang Zhou, Jingkang Yang, Chen Change Loy, and Ziwei Liu. Conditional prompt learning for vision-language models. In *Proceedings of the IEEE/CVF conference on computer vision and pattern recognition*, pages 16816–16825, 2022. 2

[38] Kaiyang Zhou, Jingkang Yang, Chen Change Loy, and Ziwei Liu. Learning to prompt for vision-language models. *International Journal of Computer Vision*, 130(9):2337–2348, 2022. 2, 5, 6

From Tokens to Photons: Test-Time Physical Prompting for Vision-Language Models

Supplementary Material

A. Evaluation on different architectures

To verify that the effectiveness of *MVP* does not depend on a specific prompting architecture, we further evaluate our framework on two additional backbones: (1) CLIP ViT-B/16 *without* MaPLE initialization (*i.e.*, no visual prompt tokens), and (2) CLIP ResNet50. All components of *MVP*—including feature-space distance computation, physical-view selection, and entropy-filtered aggregation—are kept identical to the main setup; only the underlying visual encoder is replaced. For fair comparison, the text prompt is initialized using the standard CLIP template, “a photo of a class”, without any learned prompt vectors.

For ViT-B/16 *without* MaPLE, we retain the identical procedure to the main experiments for computing source statistics and feature-space distances.

For ResNet50, we replace the layer-wise token statistics used for ViT with block-wise statistics by treating each Bottleneck block as an individual layer. Specifically, each block’s feature map $[B, C, H, W]$ is reshaped by flattening the spatial dimensions ($H \times W$) so that each spatial location is regarded as a token. We then compute mean and variance over the resulting (token, channel) representations and measure the feature-space affinity between these block-level statistics and the pre-computed source statistics. The affinity score is computed over the first 7 out of 16 bottleneck blocks, following the observation in [21] that ResNet requires a larger portion of its early blocks to produce representations comparable to those obtained from a much smaller number of early ViT layers.

Results are presented in Table 7 and 8. Across both backbones, the average performance of *MVP* consistently outperforms all forward-only and prompt-based TTA baselines, demonstrating that its effectiveness does not depend on the choice of visual backbone or on the presence of tuned prompt vectors.

B. Additional implementation details and full results about main evaluation

In addition to 4.1 in the main paper, we provide detailed implementation configurations. All baselines are initialized with MaPLE [17] weights, which place learnable prompt vectors in both the text and visual encoders up to the third layer. To ensure that each method operates as originally intended, we restrict gradient updates to only the textual prompt vectors (`prompt_learner.ctx`) for all prompt-based TTA baselines except PromptAlign [1].

Table 5. Ablation on aggregation strategies.

Aggregation	IN-ES	IN-ES-Diverse
Marginalized Prob.	87.80	66.72
Hard Voting (Ours)	87.85	67.28

PromptAlign is the only method allowed to update visual prompt vectors, as its objective explicitly relies on adjusting visual features for cross-modal alignment. For all other TTA baselines, no gradients flow into the visual encoder, and only the text-encoder input prompts are adapted at test time.

We also report the full accuracy results across individual lighting environments for both ImageNet-ES [2] and ImageNet-ES-Diverse [3]. Table 9 summarizes detailed accuracies under the three evaluation settings used in the main paper—AE, AE + photometric augmentations, and Lens-based selection—across all lighting conditions.

C. Comparison of aggregation strategies for multi-view prediction.

The final prediction is obtained from entropy-filtered views, and we compare two aggregation schemes: averaging the probability distributions across all views (marginalized probability) and applying zero-temperature softmax (hard voting). The results are summarized in Table 5, where hard voting consistently outperforms marginalized aggregation. This indicates that augmented-view predictions suffer from overconfidence issues, making marginalized probability sensitive to noisy or miscalibrated views, whereas hard voting remains more robust to such noise by relying on label-level consistency.

D. Runtime latency

Fig 9 presents the runtime latency breakdown for baseline TTA methods and *MVP* on ImageNet-ES-Diverse. All methods adopt CSA2 ($M=6$) to balance between capture cost and overall latency. The *Parameter Selection* stage corresponds to selecting the most confident physical view in Lens and selecting the top-5 physical views with the highest source-affinity scores in *MVP*. Prompt-based TTAs incur additional forward and backward passes to update prompt vectors during inference, while training-free TTAs and *MVP* do not require such gradient-based operations. *Inference* stage denotes the end-to-end forward pass that pro-

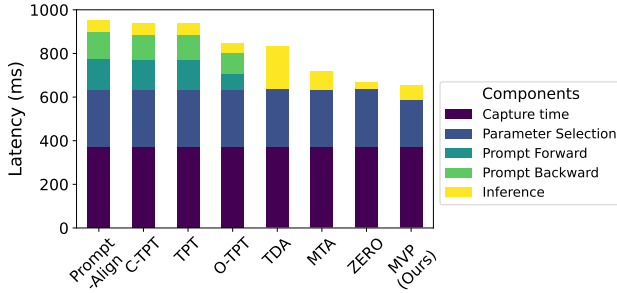


Figure 9. Total latency (ms) of adaptation and inference

duces the final prediction for a single test sample. Latency for parameter selection is averaged across all 27 parameter configurations, while latency for the remaining procedures is computed by measuring per-sample runtime over 1,000 test samples and reporting the average. The total latency is illustrated in Fig 6.

E. CSA details

CSA (Candidate Selection Algorithm) is a pre-selection strategy designed to reduce redundant capture time before performing sensor control [3]. It provides three approaches for selecting M candidate parameter configurations from the full set of available sensor-control options.

CSA1 performs uniform random sampling across all parameter configurations.

CSA2 adopts a grid-based random selection strategy to ensure even coverage of the parameter space. The full 3D (ISO, shutter speed, aperture) parameter space is partitioned into several grids, and one candidate is sampled from each grid until M selections are made. Since parameters within the same grid are close in value, the resulting captures tend to exhibit similar image qualities. The number of grids is pre-defined as 1^3 for $M = 6$ in [3], but for fairer exposure variability, we adjust this to 2^3 grids in our evaluation.

CSA3 selects M parameter configurations with the lowest capture cost, determined primarily by shutter speed. When multiple configurations have identical costs, the algorithm breaks ties randomly.

Table 10, 11, and 12 present extended CSA results, including those from Table 2, evaluated across various values of M . For all experiments, we report the average performance over three runs with different random seeds. CSA3 places the strongest emphasis on efficiency among the three strategies, which leads to severe performance degradation especially under low-illumination conditions. Consequently, its accuracy drops sharply as M decreases, and we therefore evaluate CSA3 only for $M = 21$ and $M = 18$.

MVP consistently achieves the highest accuracy across all evaluated values of M .

Table 6. CLIP-ViT-B-16 initialized with MaPLE [17] weights

# of physical views	Method	IN-ES	IN-ES-Diverse
Single-view ($k = 1$)	Lens + hard voting	84.30	65.05
	<i>MVP</i>(ours)	85.45	65.33
Multi-view ($k = 5$)	Lens + hard voting	86.95	66.78
	<i>MVP</i>(ours)	87.85	67.28

F. Controlled Comparison of Physical View Selection under Fixed k

Table 6 presents a controlled comparison in which the number of selected physical views (k) and the aggregation strategy over filtered digital view predictions are fixed, while only the physical view selection criterion is varied. This setting allows us to isolate the effects of the two key components of *MVP*: (i) using multiple physical views as a new augmentation axis, and (ii) the proposed source affinity criterion.

Regardless of whether $k = 1$ or $k = 5$, the source affinity score of *MVP* consistently outperforms the confidence score used in Lens [3], as it does not rely on physical views that the model may judge overconfidently. Instead, it selects physical views that are more aligned with the distribution learned by the model and therefore better understood by it, leading to higher performance.

In addition, Lens [3] also benefits from multi-view aggregation, confirming the augmentation effect of using multiple physical views and further supporting the necessity of multi-physical view modeling, as emphasized in our approach.

G. LDA visualization on more samples

Figure 10 show additional LDA projection visualizations for each lighting condition in ImageNet-ES and ImageNet-ES-Diverse, along with the corresponding top-5 camera parameters ranked by affinity score.

H. Additional qualitative analyses

Figure 11 provides additional qualitative comparisons illustrating the differences between the views selected by ZERO with Lens and *MVP*, in addition to figure 7. These additional qualitative examples further confirm that the lack of diversity inherent in a limited physical sensor space cannot be compensated for by digitally augmented views alone, consistently highlighting the necessity of leveraging multiple physically captured measurements.

I. ImageNet-ES/ImageNet-ES-Diverse details

ImageNet-ES [2] and ImageNet-ES-Diverse [3] are benchmarks designed to evaluate robustness under sensor-level covariate shifts induced by variations in lighting conditions and camera parameters. Their test sets consist of 64k and 192k samples, respectively.

The two datasets differ primarily in object presentation: ImageNet-ES captures a monitor displaying the objects, treating them as light-emitting sources, while ImageNet-ES-Diverse captures printed images of the objects, enabling more realistic evaluation under ambient lighting. Furthermore, ImageNet-ES includes only two lighting conditions (e.g. light-on, light-off), whereas ImageNet-ES-Diverse provides six diverse illumination settings.

Both benchmarks share the same camera parameter protocol. The *Auto-Exposure (AE)* set contains five captures per scene using the camera’s automatic exposure mode, while the *parameter-controlled* set contains 27 captures obtained under controlled combinations of ISO, shutter speed, and aperture—three levels each (ISO: {250, 2000, 16000}, Shutter: {1/4'', 1/60'', 1/1000''}, Aperture: f/5.0, f/9.0, f/16). Example samples from both datasets are shown in Fig. 12.

Table 7. Detailed results on ViT-B/16 backbone *without* MaPLe

Auto Exposure										
Method	ImageNet-ES			ImageNet-ES-Diverse						
	L1	L5	Average	L1	L2	L3	L4	L6	L7	Average
CLIP	50.92	47.04	48.98	38.50	37.88	39.38	39.02	36.20	34.92	37.65
TPT	54.65	50.44	52.56	40.80	40.72	42.04	40.74	38.32	36.96	39.93
C-TPT	51.72	47.88	49.80	38.86	38.56	40.26	39.12	37.02	34.76	38.10
O-TPT	51.06	46.84	48.95	38.30	37.40	39.02	38.08	35.82	33.92	37.09
MTA	54.42	50.60	52.51	40.66	39.52	40.82	40.38	38.22	36.78	39.40
TDA	54.44	50.08	52.26	38.74	38.40	39.88	39.42	36.24	35.46	38.02
ZERO	56.38	51.38	53.88	39.80	39.60	40.10	39.48	37.60	35.44	38.67
with Lens										
Method	ImageNet-ES			ImageNet-ES-Diverse						
	L1	L5	Average	L1	L2	L3	L4	L6	L7	Average
CLIP+Lens	82.70	82.20	82.45	63.30	61.40	61.70	60.60	61.00	58.80	61.13
TPT	82.80	82.00	82.40	63.70	62.40	62.20	61.30	61.20	59.40	61.70
C-TPT	82.80	82.20	82.50	63.60	61.90	62.50	60.60	61.40	59.20	61.53
O-TPT	82.70	81.80	82.25	63.10	61.30	62.10	60.60	60.80	59.30	61.20
MTA	82.60	82.10	82.35	63.70	61.90	62.40	60.80	60.70	59.30	61.47
TDA	82.70	82.40	82.55	62.20	61.10	61.20	60.70	60.20	58.70	60.58
ZERO	82.90	82.40	82.65	63.60	61.20	62.10	61.70	59.90	58.80	61.22
MVP (ours)	85.30	84.30	84.80	65.30	64.80	65.50	64.20	63.40	62.70	64.32

Table 8. Detailed results on ResNet50 backbone

Method	Auto Exposure									
	ImageNet-ES			ImageNet-ES-Diverse						
	L1	L5	Average	L1	L2	L3	L4	L6	L7	Average
CLIP	35.88	31.96	33.92	17.44	17.70	18.32	17.66	16.26	15.52	17.15
TPT	39.50	36.18	37.84	21.08	21.60	21.82	21.36	20.00	18.70	20.76
C-TPT	37.62	33.12	35.37	17.74	18.06	18.74	18.06	16.56	15.74	17.48
O-TPT	36.08	31.68	33.97	18.34	18.24	19.02	18.52	17.26	16.46	17.97
MTA	38.52	34.90	36.71	16.76	16.52	17.36	16.34	15.20	14.22	16.15
TDA	38.62	35.16	36.89	16.16	16.26	16.86	16.32	14.24	13.60	15.57
ZERO	39.34	35.82	37.58	15.82	15.42	15.84	15.96	14.22	13.10	15.06
with Lens										
Method	ImageNet-ES			ImageNet-ES-Diverse						
	L1	L5	Average	L1	L2	L3	L4	L6	L7	Average
CLIP+Lens	73.60	73.30	73.45	40.90	41.50	39.90	38.70	38.60	37.20	39.47
TPT	73.90	73.70	73.80	41.40	41.50	40.40	39.60	39.30	37.40	39.93
C-TPT	73.70	73.40	73.55	41.30	41.20	40.20	39.60	39.30	37.60	39.87
O-TPT	73.70	73.40	73.55	41.40	41.60	40.30	39.40	39.00	37.10	39.80
MTA	74.00	73.70	73.85	41.20	41.00	39.90	39.00	38.40	37.40	39.48
TDA	72.50	73.40	72.95	40.70	39.60	39.80	38.60	37.80	36.00	38.75
ZERO	73.50	73.90	73.70	40.20	39.80	40.00	37.60	38.20	35.20	38.50
MVP (ours)	76.00	74.80	75.40	43.20	41.70	41.50	38.80	39.10	36.50	40.13

Table 9. Detailed results of main evaluation

Auto Exposure										
Method	ImageNet-ES			ImageNet-ES-Diverse						
	L1	L5	Average	L1	L2	L3	L4	L6	L7	Average
CLIP	50.92	47.04	48.98	38.50	37.88	39.38	39.02	36.20	34.92	37.65
CoOp	54.48	49.16	51.82	41.36	40.78	42.20	41.72	39.36	37.38	40.47
MaPle	54.98	50.16	52.57	40.56	39.76	41.24	40.24	38.48	36.52	39.47
TPT	58.64	52.68	55.66	42.86	41.34	43.00	41.76	39.62	38.60	41.20
PromptAlign	58.20	52.70	55.45	42.66	41.40	43.70	42.32	39.90	39.06	41.51
C-TPT	56.24	50.86	53.55	41.24	40.16	41.46	40.22	39.02	37.18	39.88
O-TPT	55.12	50.28	52.70	40.38	39.24	40.56	39.98	38.26	36.42	39.14
MTA	59.30	53.82	56.56	43.14	42.04	43.60	42.10	40.20	39.10	41.70
TDA	61.16	55.18	58.17	41.96	41.06	42.64	41.42	39.30	38.30	40.78
ZERO	59.92	54.18	57.05	40.90	40.36	41.82	40.88	38.34	37.16	39.91
Auto Exposure + Photo. Aug.										
Method	ImageNet-ES			ImageNet-ES-Diverse						
	L1	L5	Average	L1	L2	L3	L4	L6	L7	Average
TPT	52.12	47.20	49.66	42.80	40.88	42.96	41.78	38.92	37.60	40.82
PromptAlign	53.18	47.36	50.27	42.98	41.06	42.94	41.60	39.82	37.86	41.04
C-TPT	48.52	43.32	45.92	40.94	39.62	40.64	40.16	37.54	35.64	39.09
O-TPT	47.00	42.12	44.56	40.36	38.90	39.94	39.30	36.88	35.42	38.47
MTA	57.22	52.06	54.64	42.84	41.66	43.56	42.14	39.52	38.26	41.33
TDA	60.44	54.14	57.29	42.12	41.06	42.58	41.52	39.50	38.20	40.83
ZERO	59.56	53.98	56.77	41.20	39.62	41.74	40.26	38.52	37.46	39.80
with Lens										
Method	ImageNet-ES			ImageNet-ES-Diverse						
	L1	L5	Average	L1	L2	L3	L4	L6	L7	Average
CLIP+Lens	82.70	82.20	82.45	63.30	61.40	61.70	60.60	61.00	58.80	61.13
CoOp	84.80	85.00	84.90	68.20	66.10	65.70	64.20	64.40	62.30	65.15
MaPle	85.10	83.70	84.40	65.90	64.80	66.20	64.90	63.60	62.70	64.68
TPT	85.10	83.80	84.45	66.50	65.10	66.30	65.00	64.10	62.40	64.90
PromptAlign	85.70	83.80	84.75	66.90	65.30	65.70	65.50	64.00	62.00	64.90
C-TPT	85.30	83.80	84.55	66.00	64.90	66.10	64.70	63.90	62.70	64.72
O-TPT	85.30	83.70	84.50	66.00	64.80	66.10	64.50	63.80	62.60	64.63
MTA	85.40	84.00	84.70	66.20	65.70	66.50	65.20	64.20	62.70	65.08
TDA	85.80	83.80	84.80	65.90	64.40	66.30	66.00	63.60	62.90	64.85
ZERO	85.20	84.40	84.80	66.00	65.20	66.00	65.10	63.30	62.40	64.67
Ours										
MVP (ours)	87.50	88.20	87.85	69.30	67.50	69.20	66.70	66.00	65.00	67.28

Table 10. Results with CSA1 across different M .

Method	$M = 18$		$M = 15$		$M = 12$		$M = 9$		$M = 6$	
	IN-ES	IN-ES -Diverse								
Lens	84.73	63.53	84.82	63.52	84.75	61.79	84.48	60.48	83.33	55.40
+ TPT	84.82	63.94	84.98	63.86	84.88	62.22	84.90	61.03	83.77	56.33
+ PromptAlign	84.98	63.74	85.25	63.82	84.95	62.03	84.82	61.01	84.03	56.24
+ C-TPT	84.88	63.56	84.83	63.56	84.85	61.90	84.83	60.66	83.65	53.52
+ O-TPT	84.75	63.39	84.75	63.41	84.77	61.66	84.57	60.34	83.43	51.06
+ MTA	85.18	64.09	85.23	64.09	85.37	62.44	85.12	61.17	84.02	56.51
+ TDA	85.22	63.81	85.37	63.53	85.30	61.71	85.12	60.64	84.23	56.02
+ ZERO	85.43	63.50	85.75	63.38	85.43	61.49	85.23	60.03	84.60	55.59
<i>MVP</i> (ours)	87.82	66.02	87.57	65.97	87.27	63.79	86.40	62.27	85.40	57.49

 Table 11. Results with CSA2 across different M .

Method	$M = 18$		$M = 15$		$M = 12$		$M = 9$		$M = 6$	
	IN-ES	IN-ES -Diverse								
Lens	84.62	63.31	84.52	63.21	84.28	63.29	84.43	61.10	84.38	61.76
+ TPT	84.52	63.78	84.47	63.66	84.28	63.78	84.48	61.54	84.55	62.49
+ PromptAlign	84.65	63.48	84.52	63.73	84.25	63.67	84.60	61.53	84.32	62.56
+ C-TPT	84.72	63.33	84.65	63.31	84.47	63.41	84.60	60.97	84.68	61.83
+ O-TPT	84.62	63.29	84.50	63.22	84.37	63.27	84.53	60.48	84.42	61.27
+ MTA	84.98	63.89	84.87	63.89	84.88	64.04	84.95	61.80	85.10	62.74
+ TDA	84.83	63.52	85.00	63.23	84.82	63.36	84.38	61.26	84.70	62.08
+ ZERO	85.28	63.19	85.10	63.06	84.70	63.16	84.75	60.86	84.60	61.96
<i>MVP</i> (ours)	87.68	65.68	87.48	65.44	86.90	65.47	86.92	63.09	86.65	63.79

 Table 12. Results with CSA3 across different M .

Method	$M = 21$		$M = 18$	
	IN-ES	IN-ES -Diverse	IN-ES	IN-ES -Diverse
Lens	84.98	61.67	85.00	54.38
+ TPT	85.05	62.29	85.15	55.32
+ PromptAlign	85.25	62.37	85.40	55.40
+ C-TPT	85.10	61.91	85.10	54.58
+ O-TPT	85.03	61.77	85.05	54.40
+ MTA	85.33	62.62	85.30	55.30
+ TDA	85.28	62.33	85.05	54.93
+ ZERO	85.62	61.69	85.90	54.28
<i>MVP</i> (ours)	87.87	64.41	87.70	55.92

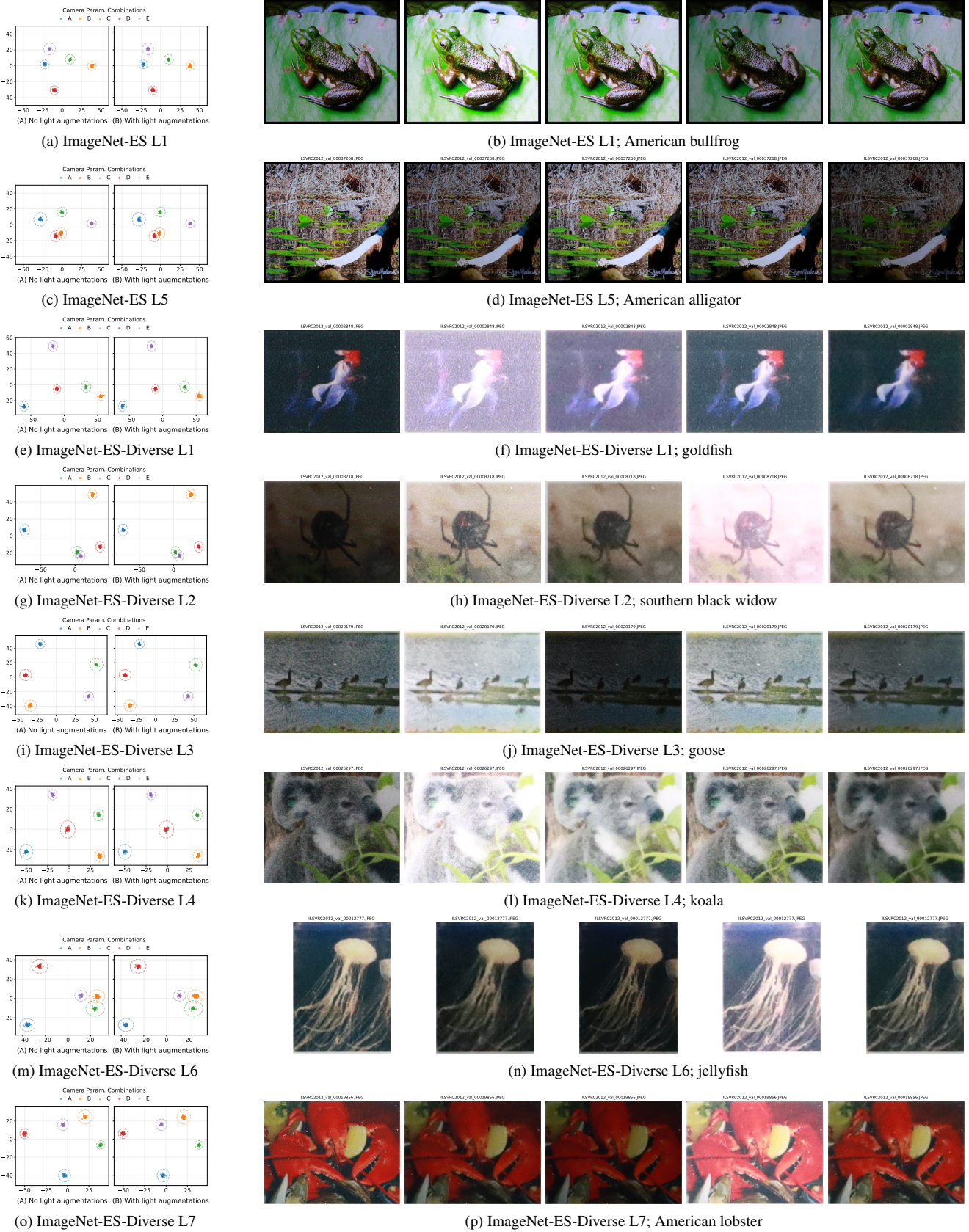


Figure 10. Additional LDA Projection Visualizations by Light Condition



(a) Remote Control



(b) Bathtub



(c) Pretzel



(d) Trolleybus



(e) Cliff Dwelling

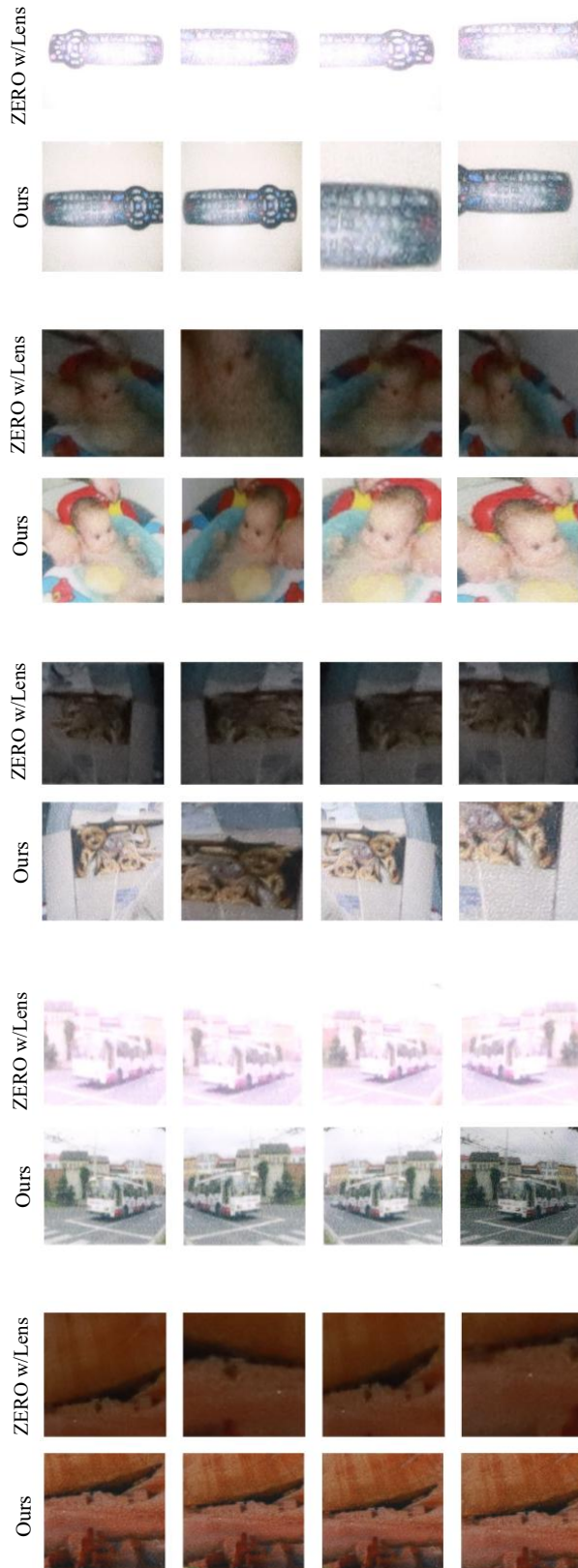


Figure 11. Additional qualitative results

Dataset	ImageNet-ES		ImageNet-ES-Diverse					
	L1	L5	L1	L2	L3	L4	L6	L7
Light								
Auto Exposure								
								
								
								
								
								
								
Parameter Control								
								
								
								
								
								
								

(a) Class name: Persian cat

Dataset	ImageNet-ES		ImageNet-ES-Diverse					
	L1	L5	L1	L2	L3	L4	L6	L7
Auto Exposure								
								
								
								
								
								
								
								
								
								
Parameter Control								
								
								
								
								
								
								
								
								
								

(b) Class name: Dragonfly

Dataset	ImageNet-ES		ImageNet-ES-Diverse						
	L1	L5	L1	L2	L3	L4	L6	L7	
Light									
Auto Exposure									
Parameter Control									
									
									
									
									
									
									
									
									
									
									
									
									
									
									
									

(c) Class name: Magnetic compass

Figure 12. Additional qualitative results